This article has been accepted for publication in a future issue of this journal, but has not been fully edited. Content may change prior to final publication. Citation information: DOI 10.1109/TPEL.2021.3064902, IEEE Transactions on Power Electronics

# Highly Efficient 11.1 kW Wireless Power Transfer Utilizing Nanocrystalline Ribbon Cores

Daniel E. Gaona, *Student Member, IEEE*, Chaoquiang Jiang, *Member, IEEE*, and Teng Long, *Member, IEEE*

***Abstract*— Nanocrystalline alloys have been recently considered as an alternative to ferrite as the magnetic cores in inductive power transfer systems due to their superior properties such as higher saturation flux density and permeability. They are also less brittle, more stable to temperature variations, and have a higher thermal conductivity. To take advantage of these properties, a dedicated design approach is required, different from the one used for ferrite cores. In this paper, special considerations and methods for the design of nanocrystalline ribbon cores are presented. An 11.1 kW pad is designed and compared with one with identical ferrite cores. Results show that IPT pads with nanocrystalline ribbon cores yield superior magnetic performance in terms of inductances and coupling factors. Higher efficiency and power density were also achieved with the proposed design. Furthermore, compared to ferrite-based pads, they showed lower leakage flux and a superior stability to temperature variations.**

***Keywords—Inductive power transfer, nanocrystalline ribbon, magnetic materials, magnetic cores.***

## I. Introduction

Inductive power transfer (IPT) technology relies on magnetic cores to constrain the magnetic flux and to increase the magnetic coupling between charging pads. MnZn based ferrite materials such as the EPCOS [1]–[3] or K2004 [2], [4] are often used. Ferrite is a long-established material. However, it presents several drawbacks when used in IPT applications. First, it is brittle and prone to mechanical breakage. Moreover, ferrite cores have a low flux density saturation point, which presents challenges for the design of compact and high-power IPT systems [5]. Furthermore, the magnetic properties of ferrite change drastically with temperature. This complicates the design of reliable and compact IPT systems and increases the requirements for cooling.

In the last years, reducing the reliance of IPT systems on ferrite has been the focus of research. This has been done by optimizing the amount of ferrite needed in each pad as in [6] and [7] or by identifying alternative magnetic materials [8], [9]. In [8], for instance, ferrite nano-particles on a base of a polymer are used to increase the robustness of the system and reduce the reliance on brittle ferrite blocks. In [9], nanocrystalline ribbon cores are considered as a replacement of ferrite cores given the superior magnetic (magnetic saturation, permeability, Curie Temperature) and mechanical (malleability, robustness) properties of this material compared to other modern magnetic materials such as permalloy, sendust, and FE-based amorphous materials [10]–[12]. The analysis presented in [9] considered a pad that had been optimized for ferrite core bars in [3]. These bars were then substituted with ones made of nanocrystalline ribbon of two different thicknesses. Despite nanocrystalline's higher permeability, the coupling factor and mutual inductance showed only a small improvement as the air-gap between pads dominates the magnetic circuit.The efficiency of the pad, nonetheless, was considerably lower than the one achieved with ferrite core bars of the same dimensions. The rather large drop in efficiency was caused by eddy-currents induced, particularly, on the lateral faces of the core. The findings and results from [9] have led to the conclusion that the design methodology used for IPT pads with ferrite cores cannot be directly used for nanocrystalline ribbon cores. Thus, a dedicated methodology is required.

An improved design methodology is presented in this paper. As opposed to [9], this paper takes into account the unique properties of nanocrystalline ribbons. Following the new design guidelines, the eddy-current losses can be considerably reduced and designs with high power density and efficiency are possible. The design considerations required for the effective construction of IPT pads with nanocrystalline ribbon cores are presented in detail in Section III. These design guidelines are applied in the construction of a WPT2 system in Section IV. In section V, the performance of the pad is analyzed in terms of magnetic performance, efficiency, leakage flux, flux/temperature distribution, and performance under temperature variations. An IPT system of the same dimensions but with ferrite cores has been also evaluated. It is expected for the latter to underperform the pad with nanocrystalline ribbon cores given that the design methodology is not optimized for ferrite. However, the analysis of the pad with ferrite cores serves a reference and allows us to compare quantitatively the performance of both magnetic material and structures under the aforementioned conditions.

## II. Simulation Environment and Framework

### A. Definition of terms

The general structure of an IPT system is shown in Fig.1. Throughout this paper, a nominal frequency of 85 kHz is used according to the standard SAE J2954 for electric vehicle applications. The magnetic pads can be represented as a pair of loosely coupled inductors with different values of self-inductance ($L_1$ and $L_2$) and mutual inductance ($M$). The coupling factor $k = M/\sqrt{L_1 L_2}$ for such arrangements ranges between 0.15 and 0.5 depending on the magnetic design and the air gap between pads [13].

The power transfer between pads is given by (1):

$$P_{out} = V_{oc} I_{sc} Q_L = \omega I_1^2 \frac{M^2}{L_2} Q_L = P_{su} Q_L \qquad (1)$$

This work was supported in part by the UK Engineering and Physical Sciences Research Council (EPSRC) under Grant EP/R036799/1 and in part by the Companhia Brasileira de Metalurgia e Mineração (CBMM) under Grant G105565.

Daniel E. Gaona, Chaoquiang Jiang, and Teng Long are with the Department of Engineering, University of Cambridge, Cambridge, CB3 0FA, UK. (e-mail: deg32@cam.ac.uk, cj426@cam.ac.uk, tl322@cam.ac.uk (corresponding author: Teng Long)).

This article has been accepted for publication in a future issue of this journal, but has not been fully edited. Content may change prior to final publication. Citation information: DOI 10.1109/TPEL.2021.3064902, IEEE Transactions on Power Electronics



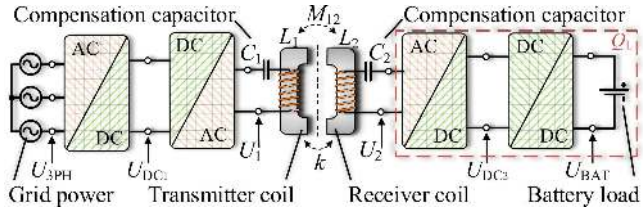


Fig. 1. Typical IPT structure. $L$: self-inductance, $M$: Mutual inductance. $k$: Coupling factor. $Q_L$: Load quality factor $Q = R_{eq}/\omega L_2$ Subscripts: 1: Transmitter, 2: Receiver inductance.

where, $V_{oc}$ and $I_{sc}$ refer to the open-circuit voltage and short-circuit current in the secondary due to a current $I_1$ circulating in the primary. Here, $Q_L$ is the quality factor of the equivalent load which ranges from 4 to 6 depending on the load [13]. The uncompensated power $P_{su}$ is the product of $V_{oc}$ and $I_{sc}$ and it is used as a metric of the effectiveness of the pad's design. Another metric is the maximum power transfer efficiency which is given by (2) for a series compensated system [14]:

$$\eta_{max} = \frac{k^2 \cdot Q^2}{\left(1 + \sqrt{1 + k^2 \cdot Q^2}\right)^2} \approx 1 - \frac{2}{kQ} \tag{2}$$

Here, $Q = \sqrt{Q_1 Q_2}$ is the geometric mean of the quality factors of the transmitter and receiver coils respectively. The quality factor of the coil is the ratio between its reactance and resistance: $Q_i = \omega L_i / R_i$.

### B. Methodology: FEM Simulation

In this paper, FEM simulations using ©COMSOL are used to calculate the values of self and mutual inductances, core losses, and magnetic flux distributions. In general, FEM simulations yield high accuracy as validated in [1], [2], [9]. The discrepancy between simulation and experimental measurements are below 8%. For the experimental validation, Hitachi Metals Finemet FT-3M is used for the nanocrystalline ribbon cores. The electromagnetic properties of the nanocrystalline ribbon core used in this work are listed in Table I.

*1) Simulation of laminated nanocrystalline ribbon cores:* The methodology for simulating laminated nanocrystalline cores is presented in [12] for inductors and in [9] for IPT cores. This method defines the equivalent permeability $\mu_{eq}$ and conductivity $\sigma_{eq}$ of the material as a tensor [15]. Thus,

Table I. FINEMET AND N87 ELECTROMAGNETIC PARAMETERS

| **Parameter** at 85 kHz | **Nanocrystalline Finemet** | **Ferrite N87** |
|---|---|---|
| Density w/o resin coating | 7300 kg/m$^3$ | 4850 kg/m$^3$ |
| Density with resin coating | 5717 kg/m$^3$ | NA |
| Filling/Stacking Factor $F$ | 0.77 | 1 |
| Ribbon thickness $t_{rib}$ | 18 $\mu$m | NA |
| Core thickness/Ribbon width $w_{rib}$ | 4 mm | 4 mm |
| Resisitivity $1/\sigma$ | 1.2 $\mu\Omega$m | 10 $\Omega$m |
| Relative Permeability (Bulk) | 23000 | 2300 |
| $\sigma_{eq,z} = \sigma_{eq,x}$ | 6.42E5 S/m | 0.1 S/m |
| $\sigma_{eq,y}$ | 22 S/m | 0.1 S/m |
| $\mu_{eq,z} = \mu_{eq,x}$ | 17652 | 2300 |
| $\mu_{eq,y}$ | 4.34 | 2300 |

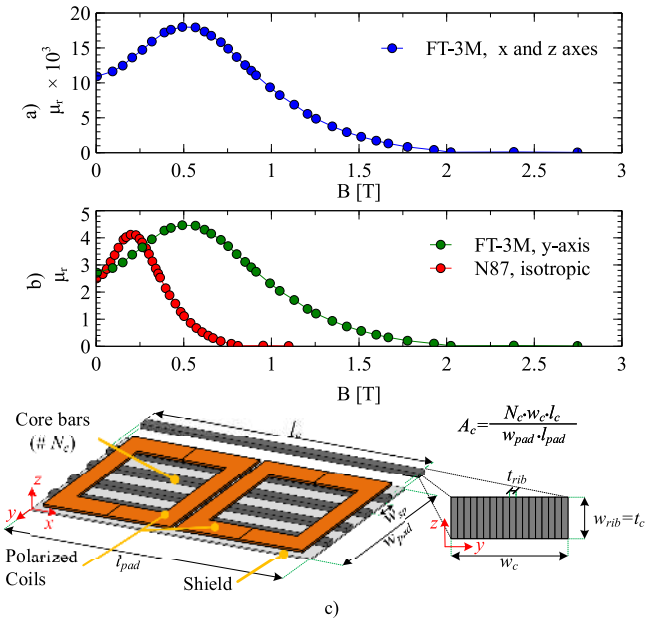


Fig. 2. Relative permeability $\mu_r$ as a function of the flux density for $b$) ferrite (isotropic) and nanocrystalline ribbon cores (anisotropic): $a$) $\mu_{r,x}$, $\mu_{r,z}$, and $b$) $\mu_{r,y}$. $c$) Depiction of the pad and the $x$, $y$, and $z$ axes. Subscripts, $rib$ : Ribbon, $c$ : core, $pad$ : complete pad. $w_{sp}$ : spacing between cores.

the conductivity for each axis ($x$, $y$, or $z$) is given by (3) [15]:

$$\sigma_{eq,z} = \sigma_{eq,x} = F\sigma, \quad \sigma_{eq,y} \approx \frac{\sigma}{F}\left(\frac{t_{rib}}{w_{rib}}\right)^2 \tag{3}$$

where $\sigma$ is the conductivity of the bulk material, $t_{rib}$ is the ribbon thickness, $w_{rib}$ is the ribbon width, and $F$ is the stacking factor, as shown in Fig.2$c$). Similarly, the permeability tensor is given by (4) [12]:

$$\mu_{eq,y} = \frac{\mu\mu_0}{F\mu_0 + (1-F)\mu}$$
$$\mu_{eq,z} = \mu_{eq,x} = F\mu + (1-F)\mu_0 \tag{4}$$

Here, $\mu$ refers to the bulk permeability whilst $\mu_0$ refers to the permeability of free-space. To account for saturation, the BH-curve of the bulk material is required. The BH-curve is scaled in each axis according to (4) as shown in Fig.2$a$) and Fig.2$b$) [16].

To ensure an adequate accuracy, the mesh size of the critical elements (core sides) must be lower than half the skin depth of the equivalent core which is given by (5):

$$\delta_{nano,eq} = \sqrt{\frac{1}{\pi f \mu_0 \mu_y \sigma_x}} \approx 1 \text{ mm} \tag{5}$$

In this case, a mesh size between $0.3 - 0.4$mm was considered at the critical boundaries while a courser mesh was defined elsewhere. Within the core, the maximum element size was defined as 5 mm.

### C. Estimation of Power Losses

*1) Core Losses:* Core losses are estimated from FEA simulations using the Steinmetz method [1]–[4], [9], [14]. For a fixed frequency (85 kHz), the power loss per unit volume is given by $P_v = C'_m B^\beta$;where, $B$ is the magnetic flux density whereas $C'_m$ and $\beta$ are empirical values obtained

This article has been accepted for publication in a future issue of this journal, but has not been fully edited. Content may change prior to final publication. Citation information: DOI 10.1109/TPEL.2021.3064902, IEEE Transactions on Power Electronics



Table II. STEINMETZ PARAMETERS

| Material | Thickness $t_{rib}$ | $C'_m$ [ $\mathrm{W/m^3/T^\beta}$] | $\beta$ |
|---|---|---|---|
| Finemet FT-3M | 18 $\mu$m | $4.45 \times 10^6$ | 1.87 |
| N87 | | $2.54 \times 10^7$ | 2.3 |

from the data-sheet of each material. The parameters for ferrite N87 and Finemet are detailed in Table II.

These coefficients $C'_m$ and $\beta$ consider only flux paralleled to the ribbon ($x$-axis in Fig.2$c$)). Perpendicular flux in the $y$-axis is not considered. These losses caused by these perpendicular flux are estimated via FEM simulations.

*2) Copper losses:* For the copper losses including proximity and skin effects, the analytic method presented in [14] and [9] is used. Copper losses are not estimated via FEM simulations as to do so, every individual turn ought to be geometrically defined. Thus, a homogenized multi-turn coil cannot be used which increases the complexity and computation time of the model and can lead to convergence problems.

## III. DESIGN CONSIDERATIONS FOR NANOCRYSTALLINE RIBBON CORES IN IPT APPLICATIONS

The next subsections present particular considerations regarding the design of nanocrystalline ribbon cores. An exemplary Double-D is used for the analysis. This pad consists of 22-turns of litz wire with 5 mm in diameter. The pad size is 430 mm×650 mm and the air gap between pads was defined as 200 mm.

### A. Comparison of Flux Distribution within the Core

A comparison of the flux distribution in the core of an IPT system is shown in Fig.3 for N87 and nanocrystalline ribbon cores. Due to the isotropic properties of the ferrite, the flux distribution is practically uniform along the $y$ and $z$ axes of the bar. Along the $x$-axis, the center of the bar shows higher flux density as this section offers a shorter flux path between two coils; i.e., nearly all flux paths cross the center of the core.

The flux density is not uniform in the $y$-axis for the nanocrystalline cores. This is due to its anisotropic permeability. The flux entering the lateral faces (defined as the surfaces of the $xz$ plane shown in Fig.2$c$) and Fig.3) of each bar travels mostly along the outermost ribbons. These ribbons will show higher flux density and might saturate when exposed to large perpendicular magnetic flux. The distribution of the flux density along the $z$ and $x$ axes is similar to that of the ferrite cores.

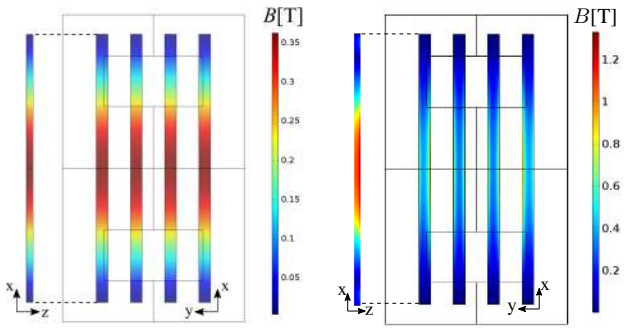


(a) N87 (b) Nanocrystalline $\sigma_{eq} = 0$

Fig. 3. Flux density distribution for $a$) N87 $b$) nanocrystalline core bars at an air gap of 100 mm. Result obtained from [9].

### B. Core Dimension (Ferrite) vs. $P_{su}$ and $B_{max}$

It is a common practice to use segregated ferrite bars rather than single-piece plates in IPT systems. Bars are less fragile and the space between bars can be used as a cooling channel with a fan placed at the end of the bar [2]. The dimensions of the bars have an impact on the coupling factor $k$, power transfer capability of the pad $P_{su}$, and maximum flux density in the cores $B_{max}$. Fig.4 shows the effect of core dimensions on the aforementioned parameters. Each point defines a different set of core dimensions. The dash-lines results from the change of one specific dimension ($l_c$, $N_c$, $A_c$ or $t_c$) while keeping the others fixed. These simulations consider a linear non-conductive isotropic ferrite material with a relative permeability of 2300. All the possible core dimensions were considered: percentage of the total pad area covered with core material $A_c$, core length $l_c$, core thickness $t_c$, and number of cores $N_c$. The main results are summarized next:

- **Number of cores $N_c$:** For low values of $A_c$, segmenting the core in higher number of uniformly distributed bars yields higher $P_{su}$ values. This is because a more uniform flux pattern is achieved. For large values of $A_c$, the number of cores used is less important.
- **Core length $l_c$:** There is an optimum core length for every pad. For this particular example, $P_{su}$ increases with the core bar length until the latter is close to $\sim$ 88% of the pad's length. $P_{su}$ then decreases for longer core bars. This is because longer cores increase the leakage flux in the transmitter without increasing the mutual inductance. As a result, $k$ and $P_{su}$ are both reduced.
- **Core surface Area $A_c$ and core thickness $t_c$:** Increasing $A_c$ or $t_c$ result both in higher $P_{su}$ values. However, as $A_c$ increases, the influence of $t_c$ reduces. For $A_c \geq 60\%$, the thickness of the bar has a negligible impact on $P_{su}$. Increasing $t_c$, however, reduces the flux density within the core and; i.e., $B_{max}$ in the core decreases proportionally. Consequently, $t_c$ can be increased to prevent saturation in the magnetic core [2], [3].
- **Maximum flux density vs core volume** From Fig.4$b$), it is clear that the maximum flux density $B_{max}$ is inversely proportional to the amount of core material. The maximum flux density is defined by the saturation point of the core material: $B_{max} = 0.45T$ for ferrite core and $B_{max} = 1.25T$ for nanocrystalline ribbon cores.
- **Pareto-front** For a fixed volume of core material, cer-

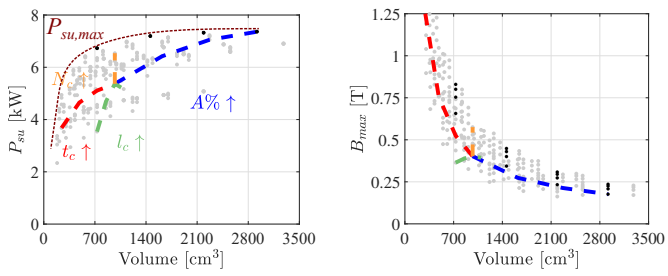


(a) N87. $P_{su}$ (b) N87. $B_{max}$

Fig. 4. $P_{su}$ and $B_{max}$ versus core volume for different core dimensions in terms of core length $l_c$, number of core bars $N_c$, core thickness $t_c$, and area of the pad cover with core material $A_c$. $i_{1,rms}$ =23 A. The dash-lines results from the change of one specific dimension ($l_c$, $N_c$, $A_c$ or $t_c$) while the others remain fixed.

This article has been accepted for publication in a future issue of this journal, but has not been fully edited. Content may change prior to final publication. Citation information: DOI 10.1109/TPEL.2021.3064902, IEEE Transactions on Power Electronics



tain core dimensions achieved higher $P_{su}$ than others. These form an envelope (Pareto-front) $P_{su,max}$ as the one shown in Fig.4$a$). The Pareto-front consists of designs with long core bars ($l_c \approx 88\%$) and high values of $A_c$. This envelope does not decrease linearly with the core volume. Contrarily, $P_{su,max}$ is fairly constant and only decays for low volumes. To optimize the utilization of core material, the core design should lie near the knee point of $P_{su,max}$, provided the material is not in saturation.

### C. Core dimension (nanocrystalline ribbon) vs. Power losses

Fig.5 compares the power transfer capability of the pad ($P_{su}$) as well as the losses of ferrite-based and nanocrystalline-based cores in terms of percentage of the pad's area covered by core material for different core thicknesses and the number of cores. The most important findings are listed below:

- **Inductances and $P_{su}$:** Slightly higher inductance and $P_{su}$ values can be achieved with nanocrystalline ribbon cores due to their higher permeability. However, the improvement is minimum as the air gap between the pads dominates the reluctance of the magnetic circuit. [9].
- **Hysteresis/Magnetic losses $P_{mag}$:** Despite the lower values of Steinmetz coefficients, hysteresis power losses ($P_{mag}$) in the nanocrystalline cores are slightly higher than that in ferrite cores. This is due to the higher hysteresis losses at the lateral faces of the core bars which have a higher flux density. As $A_c$ increases, $P_{mag}$ decreases along with the flux density. Thicker cores result also in lower flux densities and losses.
- **Eddy-current/Electrical losses $P_{elec}$:** Although almost negligible for ferrite cores, eddy-current losses are considerably high for nanocrystalline cores. To reduce these losses, the flux entering the lateral faces of the bars must be decreased. As shown in Fig.5, this can be achieved by: 1) increasing the number of cores, 2) increasing $A_c$, or 3) using thinner cores.

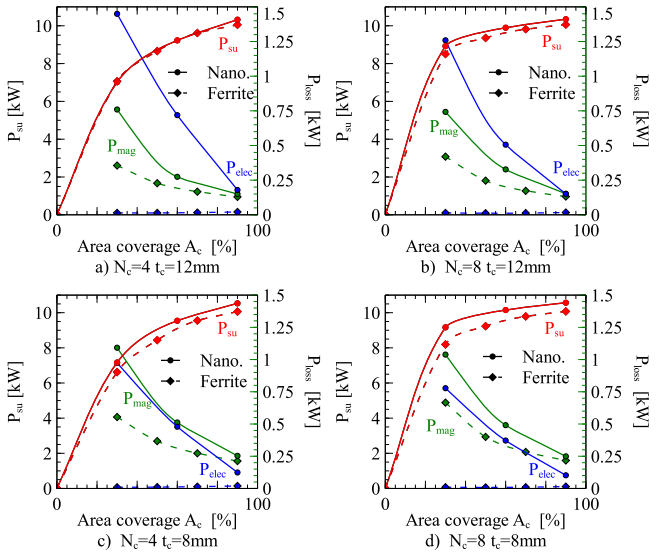


Fig. 5. Power transfer capability/ uncompensated power $P_{su}$, eddy-current losses $P_{elec}$, and hysteresis losses $P_{mag}$, for a Double-D pad nanocrystalline ribbon and ferrite cores. The $x$-axis depicts the percentage of the pad's surface area covered by core material (Area coverage). Different core thicknesses $t_c$ and number of cores $N_c$ are tested. $i_{1,rms}$ =23 A.

### D. Design Guidelines for nanocrystalline cores

For IPT systems, long and single-piece magnetic cores without air gaps are advantageous; particularly for polarized pads, such as Double-D and bipolar, where the mainstream magnetic flux is conducted along with length of the core ($x$ axis). Due to its laminated nature, nanocrystalline ribbon cores of these characteristics can be constructed without compromising mechanical robustness. Since the core length has the largest impact on the power transfer capability of the pad, a length between $80\%$ and $88\%$ of the pad's length is recommended.

To reduce eddy-current losses, the core ought to cover a large portion of the pad's area. A full coverage of the pad's flux-pipe is recommended. In this case, the core thickness can be reduced to limit the volume of core material. Furthermore, thinner cores will further reduce the eddy-current loss. Thus, the core ought to be as slim as possible so long the core remains unsaturated. In practice, it is challenging to produce thin nanocrystalline ribbon cores as the thickness of the core is given by the width of the ribbon ($w_{rib}$ in Fig.2) which is limited by manufacture constraints. The minimum width commercially available for core production is between three to four millimeters; thus, the height of the nanocrystalline ribbon core ($t_c$) is restricted to values larger than 3 mm [17], [18], [19].

These design guidelines can be also used for ferrite cores; however, ferrite cores show different dimensional limitations. First, since eddy-current loss is not a significant issue for ferrite cores, the core coverage ($A_c$) can be relaxed

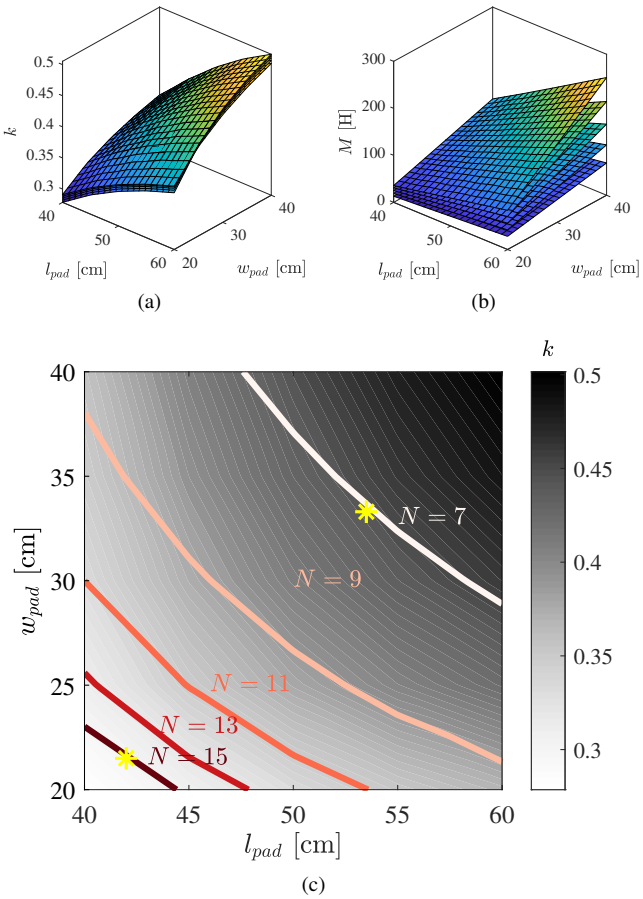


Fig. 6. Design space for the WPT3/Z1 (11 kW). $l_{pad}$, $w_{pad}$, and $N$ vs. $a$) $k$ $b$) $M$. The contour lines in $c$) define the pad size required to obtain the target mutual inductance of 64 $\mu$H. $*$: Selected designs.

This article has been accepted for publication in a future issue of this journal, but has not been fully edited. Content may change prior to final publication. Citation information: DOI 10.1109/TPEL.2021.3064902, IEEE Transactions on Power Electronics



as compared to the nanocrystalline ribbon counterpart. Second, the brittleness of the material needs to be considered. It is difficult to make ferrite cores with large footprints, particularly when the ratios length-to-thickness and width-to-thickness are large. Manufacturing ferrite cores of large footprints result in large temperature gradients across the body which result in high stress and ultimately in product cracking [5]. Thus, core bars or core plates made of an array of smaller tiles are better alternatives. Due to manufacturing tolerances, attempts to reduce the air gaps between these tiles can lead to partial saturation and hot-spots where the air-gaps are narrower. To prevent this, it is a common practice to purposely enlarge the size of the air gaps [20]. These gaps will hamper the magnetic performance of the pad; however, in most cases, their effect is minimum as long as the gaps are kept small [20]. Their actual impact will depend on their number, their size, and the separation between transmitter and receiver pads. Nanocrystalline cores can be constructed of virtually any length. Hence, no air gaps are introduced in the mainstream flux path – $x$-axis.

## IV. Design of Nanocrystalline-based IPT pads

The design guidelines discussed in the previous section are applied here in the design of a WPT3/Z1 (11.1 kW/100 mm air gap) system. The design methodology follows a similar approach to the one presented in [2] and [14].

### A. Coil Design

The process starts by selecting the DC-link voltages in the primary and secondary sides. For this contribution, a voltage of 650 V is selected for both primary and receiver DC-links: $v_{DC,1}$ and $v_{DC,2}$. With this information, the required mutual inductance is determined from the power transfer equation (6) which applies to series-compensated IPT systems:

$$P_t = \frac{4 \cdot v_{DC,1} v_{DC,2}}{\pi^3 \cdot f^2 \cdot M} \tag{6}$$

Here, $f$ is the switching frequency (85 kHz). From (6), the value of $M$ required to transmit 11.1 kW is $\approx 57\mu$H. The inductance at the knee point of the Pareto-front $P_{su,max}$ is approximately 90% of that obtained from a full core coverage (see Fig.4). Thus, when sizing the pad, FEM simulations with full core coverage can be used with $M$ =64 $\mu$H as a target as opposed to 57 $\mu$H.

Next, the coil dimensions and number of turns $N$ need to be selected. FEM simulations are performed to obtain the design space shown in Fig.6. Fig.6$a$) and $b$) show the coupling factor $k$ and mutual inductance $M$, respectively, for different pad dimensions and number of turns. Here, $k$ increases with the pad area, and it is practically unaffected by the number of turns. $M$, on the other hand, is directly proportional to both the pad's area and the number of turns. For every value of $N$, it is possible to determine the pad dimensions that result in the required value of $M$. These possible pad designs are depicted as contour-lines in Fig.6$c$). At first, two possible designs, shown in Fig.6 with ($*$) are first considered: with a larger footprint (530 mm×340 mm) and fewer turns ($N$ = 7), and one with a smaller footprint (420 mm×210 mm) and more turns ($N$ = 15). The core design for both arrangements is discussed next.

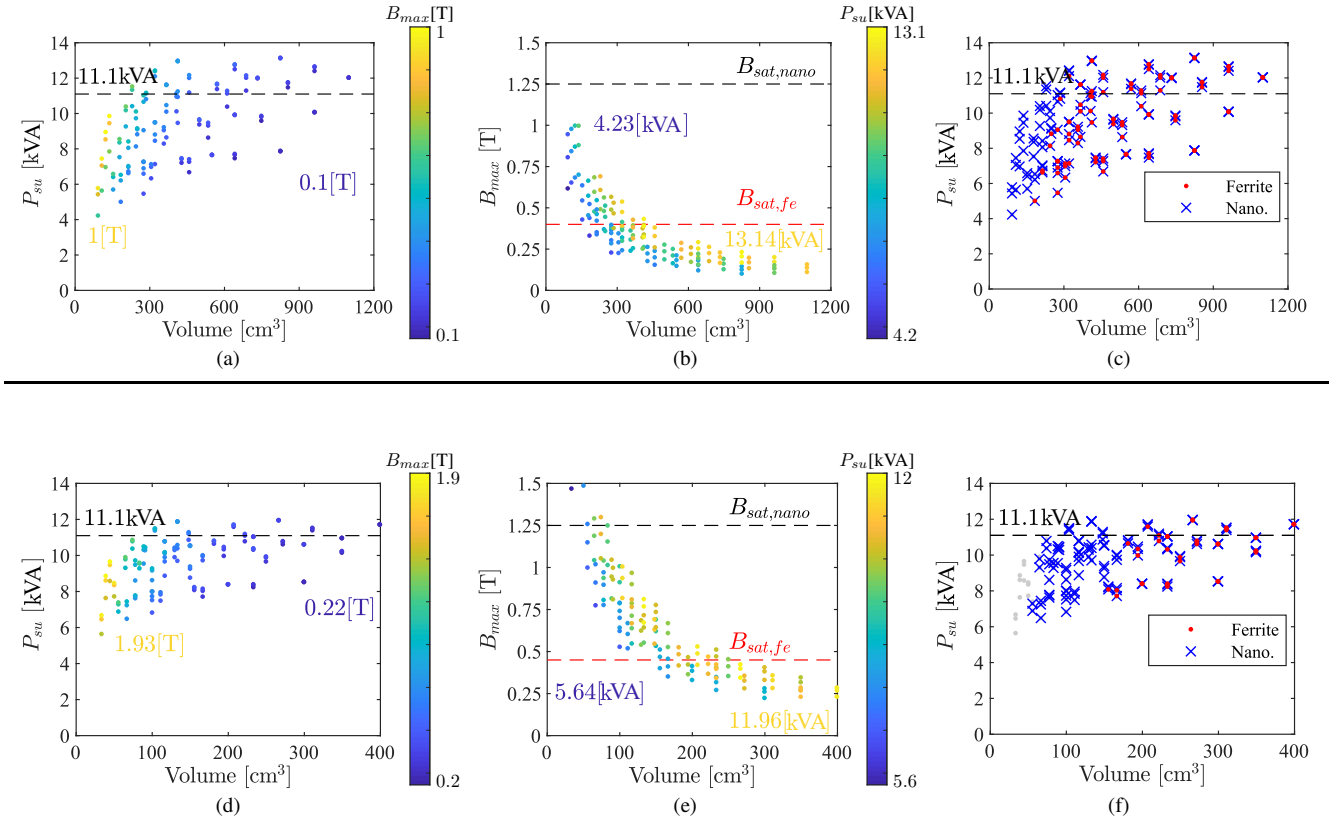


Fig. 7. Parametric sweep varying the dimensions of the core. $a$), $c$) and $e$) correspond to a 530 mm×340 mm pad with $N$ = 7 and. $b$), $d$), and $f$) correspond to a 420 mm×210 mm pad with $N$ = 15. In $e$) and $f$), (x) and (•) indicate the designs that are achievable with nanocrystalline ribbon and ferrite cores respectively. The designs in gray (•) are not feasible with neither material as they required higher flux densities. $i_{1,rms}$ =30 A.

This article has been accepted for publication in a future issue of this journal, but has not been fully edited. Content may change prior to final publication. Citation information: DOI 10.1109/TPEL.2021.3064902, IEEE Transactions on Power Electronics



### B. Core Design

Two different pad sizes are considered at first. Parametric sweeps are performed for both designs varying the core bar dimensions, as shown in Fig.7. The smaller pad requires less core material; however, the flux density in the core is higher as compared to the larger pad. Hence, the saturation point of the material becomes a limiting factor. In Fig.7$e) - f$), the blue (x) and red (•) markers represent the designs achievable with nanocrystalline ribbon and ferrite cores, respectively. For pads with small footprints, designs at the knee point of the Pareto-front are feasible nanocrystalline ribbon cores but not always with ferrite cores. This is due the higher saturation point of the former. Thus, more compact and light systems can be designed with nanocrystalline cores. The smaller footprint is selected for this contribution. From the possible designs at the knee point of the Pareto-front in Fig.7$e$), the one with $A_c$ =60 %, $l_c$ =342 mm ($\sim$ 82% of the pad length), and $t_c$ =4 mm is selected. This design is therefore optimized for nanocrystalline ribbon. An identical system with ferrite cores is expected to underperform. This is validated experimentally in Section V.

Superior core-utilization factors can be achieved when the core material covers a large portion of the pad area. The same area coverage can be achieved with a single-core plate or by using more cores with different spacing between them. Fig.8 illustrates the effect that core segregation has on the power transfer capability of the pad $P_{su}$ and the core losses. In Fig.8.$a$, the total core width ($w_{ct} = N_c \cdot w_c$) is constant whereas in Fig.8.$b$, the core volume is fixed. Four bars are considered for this analysis. In both cases, $P_{su}$ decreases rapidly as the spacing increases since less core material is present below the flux-pipe. Hysteresis losses

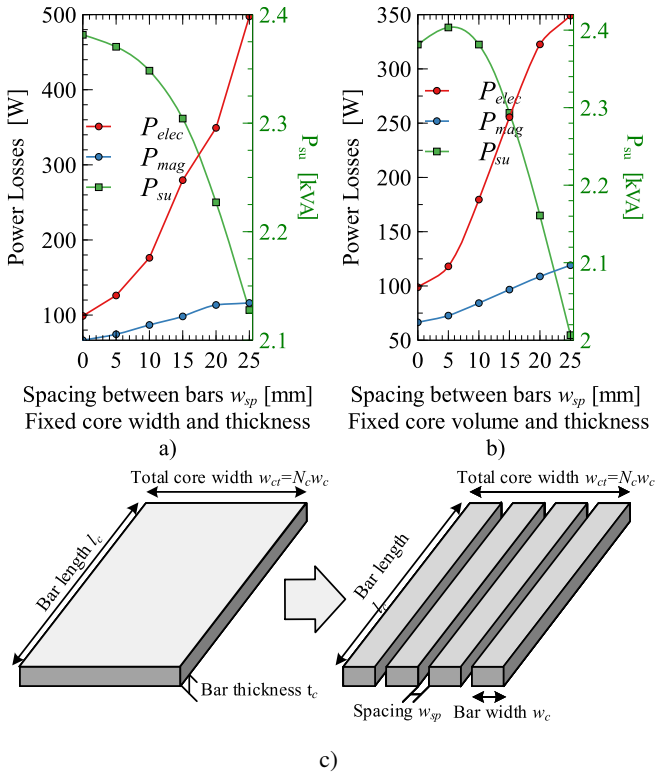


Fig. 8. Analysis of the spacing between bars on the power transfer capability of the pad $P_{su}$, eddy-current losses $P_{elec}$, and hysteresis losses $P_{mag}$. In $a$) the core width is constant while in $b$) the core volume is constant. The core thickness ($t_c$) is constant at 4 mm is constant. $c$) Definition of terms. $i_{1,pk}$ =21 A.

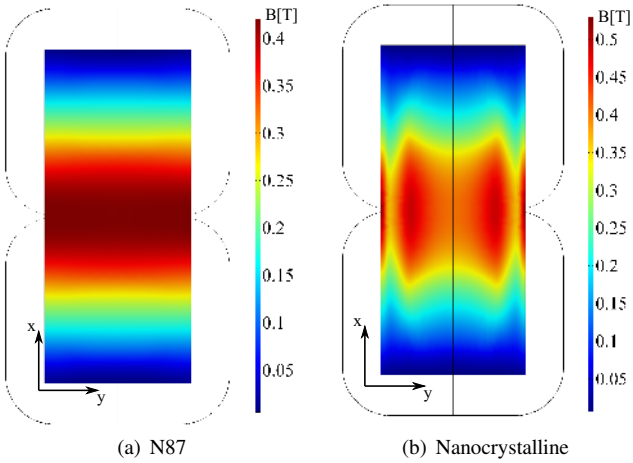


Fig. 9. Flux density distribution within the core using $a$) ferrite N87 and $b$) finemet FT-3M cores. Air gap: 100 mm. $I_{pk}$ =40 A.

($P_{mag}$) also increase due to the higher flux density at the lateral faces of the core bars. As the spacing increases, the flux is also more prone to leak into the shield. Finally and most importantly, eddy-current ($P_{elec}$) losses increase drastically with the spacing. It changes from 98 W for an entire ferrite plate to 497 W when the bars are 25 mm apart. For these reasons, non-segregated plates are preferred for nanocrystalline ribbon cores used in IPT systems. The core plate used in this paper has the following dimensions: 432 × 150 × 4mm.

### C. Flux distribution comparison

Fig.9 shows the distribution of the flux density $B$ for different core materials. Given that ferrite is an isotropic material, the flux distribution is uniform in the $y$-axis. In the $x$-axis, the flux density is lower at the edges of the core and higher at the center ($x$-axis). The anisotropic behavior of the nanocrystalline core results in a more convoluted distribution. In the $y$-axis, the sides of the core plate are exposed to higher flux densities due to fringing flux perpendicular to the ribbon [9]. Two other zones of higher flux density are found at the center of the core (below the flux-pipe). The higher flux density at these regions coincides with the inner corners of the winding. In the $x$-axis, similarly to the ferrite core plate, higher flux densities are located in the center of the core plate.

### D. Power losses comparison

Fig.10 shows a comparison of the estimated losses at 6.6 kW for the pads with ferrite and nanocrystalline ribbon

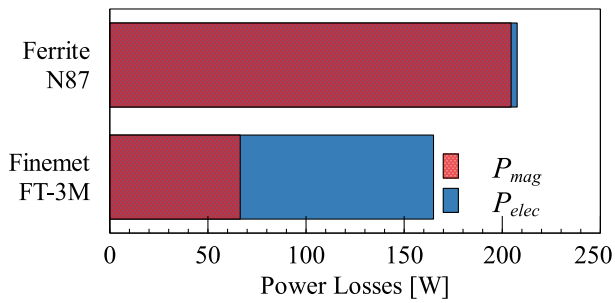


Fig. 10. Estimation of core losses with ferrite and nanocrystalline ribbon cores at 6.6 kW.

This article has been accepted for publication in a future issue of this journal, but has not been fully edited. Content may change prior to final publication. Citation information: DOI 10.1109/TPEL.2021.3064902, IEEE Transactions on Power Electronics



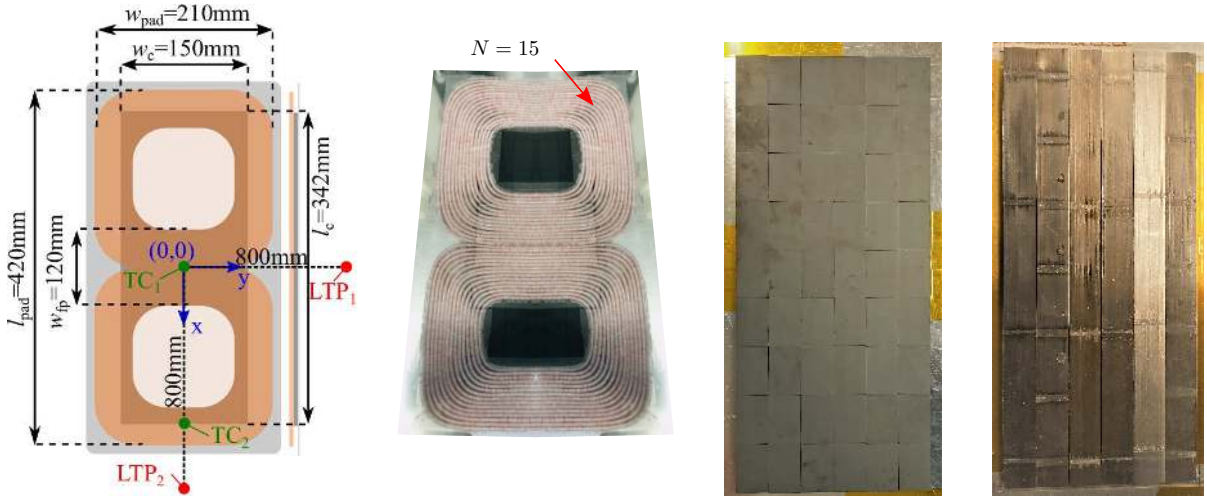


(a) Double-D pad (b) (c) Ferrite core plate (d) Finemet core plate

Fig. 11. $a$) Double-D Pad's dimensions. LTP: leakage flux test-point. TC: thermo-couple location. $b$) Depiction of the constructed pad. $c$) Ferrite core. $c$) Finemet FT-3M nanocrystalline ribbon core.

cores. For the former, most of the core loss is due to hysteresis losses. Eddy-currents are minimum and account for only $\sim 1.5\%$ of the total power loss. For the nanocrystalline ribbon cores, on the other hand, the eddy-current losses account for as much as $60\%$ of the total loss. However, the hysteresis losses are much lower. As a result, the total core loss of nanocrystalline ribbon cores is expected to be up to $21\%$ lower than that obtained with ferrite cores.

## V. Experimental validation

The design detailed in Section IV was tested experimentally when using ferrite and nanocrystalline cores of identical dimensions. For this purpose, the testbench shown in Fig.12 was used. Its main components are described next:

**Power electronics:** The transmitter coil is connected to a SiC MOSFET-based (CREE, C3M0075120K) H-Bridge. The receiver side is connected to a SiC passive full-wave rectifier (On Semiconductor, 512-FFSH40120ADNF155). A LAUNCHXL-F28379D is used for control.

**Measuring equipment:** Self and mutual inductances are measured with the impedance analyzer N4L PSM3750. A LeCroy HDO8000A is used to acquire current and voltage waveforms. A Yokogawa WT5000 is used to measure the power losses and efficiency of the coil and the entire system.

**Magnetic couplers:** The dimensions of IPT pad are depicted in Fig.11$a$). An image of the constructed pad is shown in Fig.11$b$). The coil comprises $15$ turns of Litz wire which is made of $850$ 0.1-mm-diameter strands, giving a total cross-sectional area of $6.5\ \mathrm{mm}^2$. The ferrite and nanocrystalline ribbon cores are shown in Fig.11$c$) and Fig.11$d$), respectively. The ferrite core consists of $54$ $38.1\ \mathrm{mm}\times 25.4\ \mathrm{mm}\times 4\ \mathrm{mm}$ N87 tiles. The nanocrystalline ribbon plate, on the other hand, comprises six $343\ \mathrm{mm}\times 25.4\ \mathrm{mm}\times 4\ \mathrm{mm}$ bars. Each bar is made of $18\ \mu\mathrm{m}$ Hitachi Metals FT-3M Finemet ribbons. The stacking factor is approximately $0.77$.

**Compensation circuits:** The pads are tested using series compensation circuits in both transmitter and receiver. KEMET PHE450/F450 film capacitors are for their low dissipation factor ($0.15\%$) and high voltage rating ($3000\,\mathrm{V_{DC}}$).

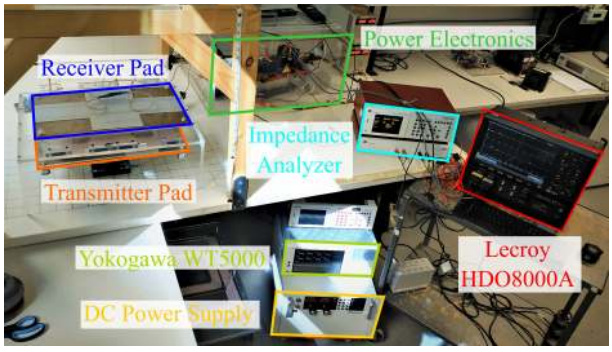


Fig. 12. Test-rig and testing equipment.

### A. Nanocrystalline Ribbon vs. Ferrite: Inductance Measurement

Fig.13 shows the measured self and mutual inductance for different pad's positions when using nanocrystalline ribbon and ferrite cores, respectively. For the former, the values of the inductance match the ones estimated with FEM simulations with a difference of less than $3\%$. For latter, the difference between the simulated and measured inductances is higher, approximately $6.5\%$. This difference is due to the fact that the simulation considered the ferrite core as a single piece whereas, in practice, the core is constituted of $54$ tiles as shown in Fig.11$c$). The measurement results lie between the simulation result without air gaps and with $50\ \mu\mathrm{m}$ air gaps.

Table III compares the magnetic perforamnce of these two materials under perfect alignment. Compared to the

Table III. Inductance measurement for different pads

| Parameter | Ferrite N87 | Finemet | Units |
|---|---|---|---|
| $L_1$ | 159.5 | 175.8 | $\mu$ |
| $L_2$ | 153.2 | 170.6 | $\mu$H |
| $M$ | 46.35 | 57.15 | $\mu$H |
| $k$ | 0.297 | 0.33 | |
| $Q=\sqrt{Q_1Q_2}$ | 340 | 286 | |
| $P_{su}$ @ $i_{1,pk}$ =21 A | 1.65 | 2.25 | kVA |

No misalignment. Clearance between pads: 100 mm.
Pad and core dimensions: Fig.11

This article has been accepted for publication in a future issue of this journal, but has not been fully edited. Content may change prior to final publication. Citation information: DOI 10.1109/TPEL.2021.3064902, IEEE Transactions on Power Electronics



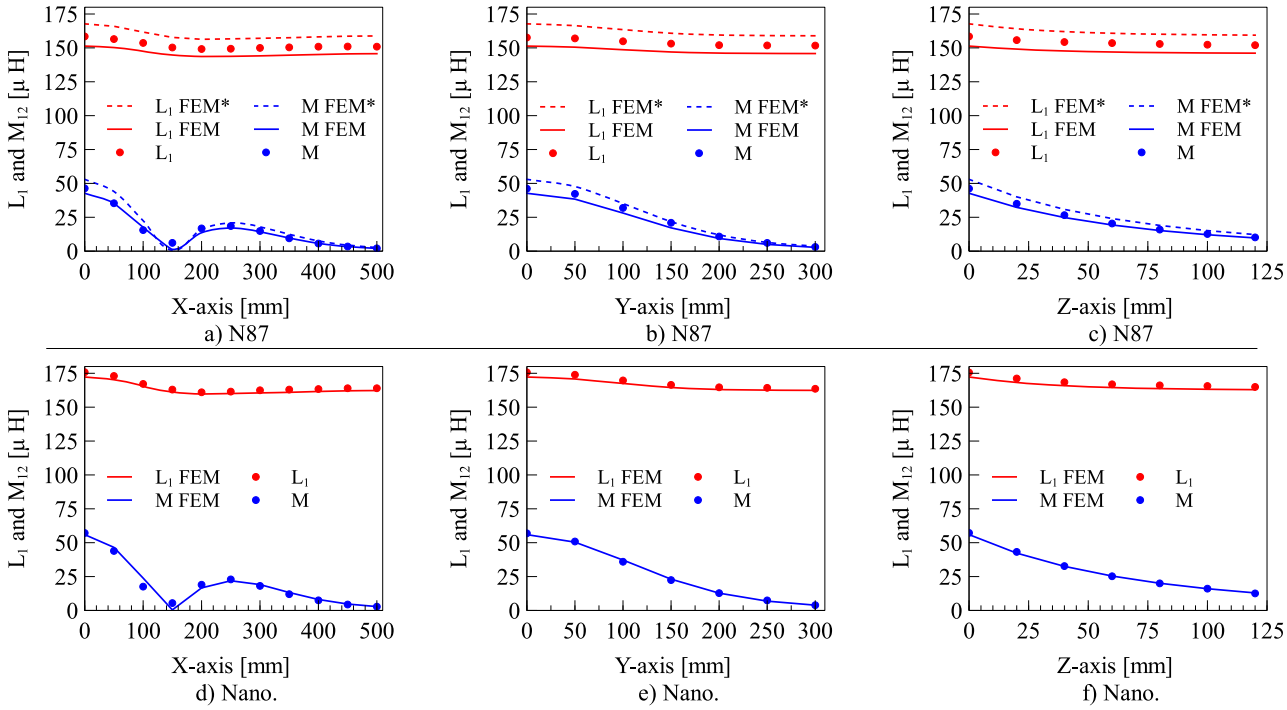


Fig. 13. Measurement of self $L_1 = L_2 = L$ and mutual $M$ inductances of the designed DD pad with nanocrystalline and N87 cores at different clearances (air gaps) between transmitter and received pads. For the ferrite cores, two simulation results are shown. One considering a core made up of ferrite tiles with $0.05$ mm separation between $(-)$ them and another considering a complete ferrite plate $(--)$. The latter is referred to as FEM*.

pad using ferrite cores, the self-inductance of the pad with nanocrystalline ribbon cores is approximately $10\%$ higher. Likewise, the mutual inductance is $23\%$ higher which results in an $11.1\%$ improvement in the coupling factor. This not only improves the power transfer capability of the pad but also its efficiency. The quality factor or the pad, measured with a phase-sensitive multimeter, is higher for the pad with ferrite cores. However, it is important to notice that this factor is measured at very low power due to the limits of the measuring device. The quality factor decreases at higher power as the core losses become more important [21]. To compare pad designs with different cores, efficiency is a better metric. This is discussed further in the next section.

### *B. Nanocrystalline Ribbon vs. Ferrite: Power Transfer and Efficiency*

Power and efficiency were measured with a clearance of $100$ mm between pads. They were both connected to the same DC-link, in recirculating power mode. Since the transmitter and receiver pads are practically identical, this operating mode allows the system to function at the optimum load matching factor which ensures maximum efficiency [9]. Under these conditions, the power transfer is given by (7):

$$P_2 = \frac{8v_{DC}^2}{\pi^2}\frac{1}{\omega M_{12}} \tag{7}$$

The power transfer increases quadratically with the DC-link voltage as shown in Fig.14$a$). The power transfer is inversely proportional to the mutual inductance. Thus, more power is transmitted with the pad with ferrite cores for the same DC-link voltage due to its lower mutual inductance. Nevertheless, more power is transferred with the pad with nanocrystalline ribbon cores for the same excitation current.

The efficiency of the system ($\eta_{DC-DC}$) is shown in Fig.14$b$). The efficiency was measured at different DC-link voltages and $25\,^{\circ}$C. The overall system's efficiency converges to $93.5\%$ for the pad with ferrite cores and to $95.5\%$ for the pad with nanocrystalline ribbon cores. The difference is attributed to the higher coupling factor and lower hysteresis losses of the nanocrystalline cores.

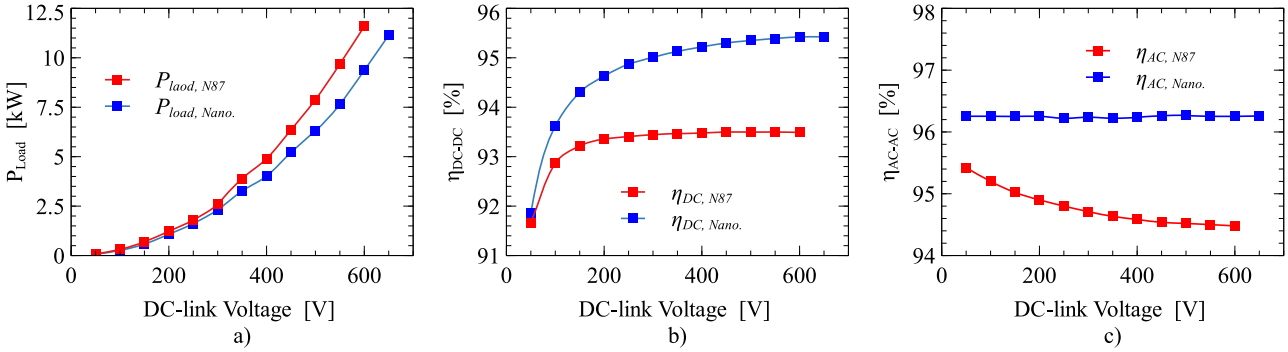


Fig. 14. Power loss measurement for Double-D pad with N87 cores and Nanocrystalline cores. $a$) Output power to the load. $b$) Overall efficiency of the system $\eta_{DC-DC}$. $c$) Efficiency of the pad without considering the power converters.

This article has been accepted for publication in a future issue of this journal, but has not been fully edited. Content may change prior to final publication. Citation information: DOI 10.1109/TPEL.2021.3064902, IEEE Transactions on Power Electronics



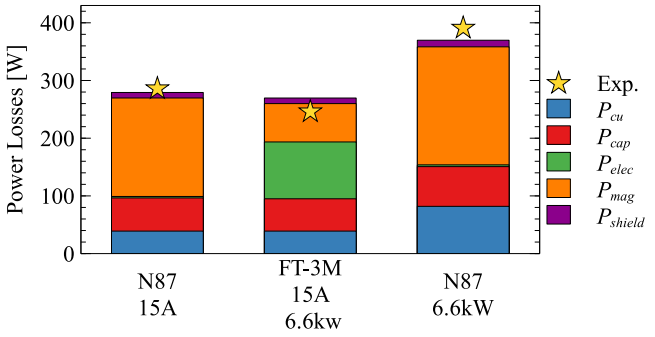


Fig. 15. Breakdown of losses in the pads with N87 and Finemet FT-3M cores. The losses are compared at the same current and the same power.

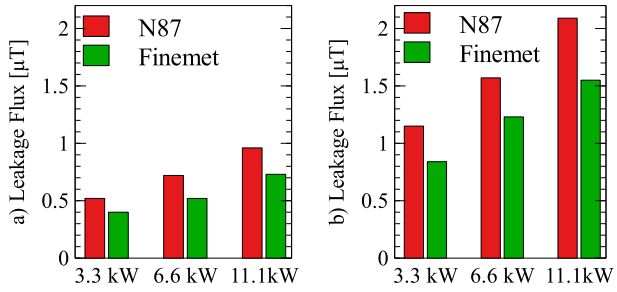


Fig. 16. Measured leakage flux at 800 mm from the center of the pad. The mid-plane between Tx and Rx is considered. Two points are selected: $a$) one parallel to $y$-axis and another one parallel to the $b$) $x$-axis. Axes are define in Fig.2.

The efficiency of the magnetic couplers (without considering the converter losses) is shown in Fig.14.*c*. The efficiency remains approximately constant at 96.26% for the pad with nanocrystalline ribbon cores. The efficiency of the pad with ferrite cores, however, starts at approximately 95.5% at low power and decreases for higher power ratings. At the rated power, 11.1 kW, it is about 94.5%. This reduction in efficiency is due to the hysteresis losses in the ferrite material which increases exponentially with the flux density. As a result, the quality factor of the coil also worsens at high power transfer. This behavior matches the analysis of the quality factor at high power presented in [22]. For both pads, at the rated power, the power converter efficiency is just above 98% thanks to soft-switching.

In [9], a pad with four spaced nanocrystalline core bars was evaluated. Its efficiency (88%) was lower than the one achieved with an identical pad with ferrite cores (94%). That design, however, did not consider the particular characteristics of nanocrystalline cores. The results, shown in Fig.14, demonstrate that nanocrystalline pads can in fact yield high efficiency when designed properly, following the guidelines discussed in Section III-D.

*a) Loss breakdown:* A breakdown of losses is shown in Fig.15 for the same excitation current and power transfer, respectively. The measured losses are also depicted in Fig.15 (*Exp.*). There is a good agreement between the estimated and measured losses in the pad which validates the modeling approach. For the pad with nanocrystalline cores, eddy-current losses are the largest component, accounting for about 30% of the total loss. Hysteresis losses correspond to 23% of the total power loss. On the other hand, for the pads with ferrite cores, the majority of the loss corresponds to the hysteresis losses. They account for approximately 58% of the total loss. Hysteresis losses in the pad with ferrite cores are about 2.6 times larger than that of the pad with nanocrystalline ribbon cores. As a result, despite having larger eddy-current losses, nanocrystalline pads show lower overall losses for the same current. When comparing the power losses at the same power rating, the results are even more clear. For the same power, the losses obtained with ferrite cores are about 59% larger than those obtained with the nanocrystalline ribbon ones.

### *C. Nanocrystalline Ribbon vs. Ferrite: Leakage*

The flux leakage was measured for pads using both ferrite and nanocrystalline ribbon cores. For the measurement, a Beehive Electronics' 100C magnetic flux probe and a Rigol's Spectrum Analyzer DSA815 were used. The Tx and Rx pads were perfectly aligned and 100 mm apart. The leakage flux was measured at a distance of 800 mm from the center of the pad and at a height of 50 mm (mid-plane between pads). The test-points are shown as LPT1 and LPT2 in Fig.11(a).

As shown in Fig.16$a$) and Fig.16$b$), the leakage flux increases with the power rating. However, due to the smaller footprint of the pad − compared to other commercial units [23]−, the leakage flux remained below 2.5 μT even at the rated power, 11.1 kW. The leakage flux for the system with nanocrystalline ribbon cores is approximately 25% lower than for the system with ferrite cores. This is attributed to the higher permeability of the core. Lower leakage facilitates the compliance of safety codes and the design of the pads with higher power ratings and densities.

### *D. Nanocrystalline Ribbon vs. Ferrite: Power Transfer and Saturation*

Nanocrystalline cores have a higher saturation point. Therefore, they can operate at higher magnetic loading. To analyze this effect the pads were tested exceeding their nominal rating of 11.1 kW (Fig.18). The distance between the transmitter and the receiver pads was adjusted to obtain the same mutual inductance with both material: 105 mm for the ferrite, and 145 mm for the nanocrystalline (a 38% larger air gap). This way, the excitation currents and the power transferred for a given DC-link voltage are the same for both pads.

For the ferrite pad, the power transfer is limited to ∼16 kW due to saturation. DC-link voltages greater than

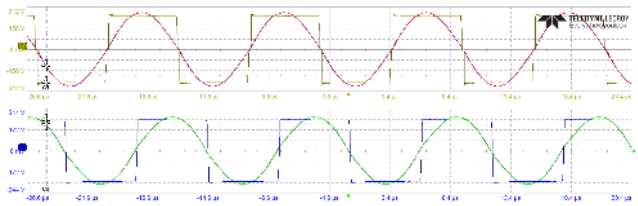

(a) $v_{DC} = 250$V

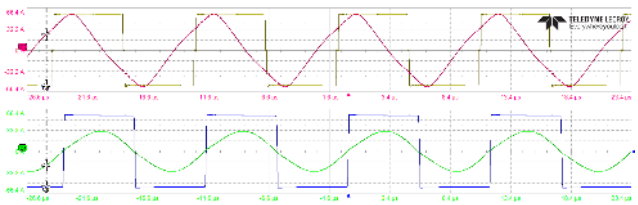

(b) $v_{DC} = 600$V

Fig. 17. Ferrite pad. Transmitter and Receiver waveforms: $V_1$ (yellow), $V_2$ (blue), $I_1$ (red), and $I_2$ (green) at $a$)$u_{DC}$ =250 V and $b$)$u_{DC}$ =600 V. Air gap between pads: ∼ 100 mm.

This article has been accepted for publication in a future issue of this journal, but has not been fully edited. Content may change prior to final publication. Citation information: DOI 10.1109/TPEL.2021.3064902, IEEE Transactions on Power Electronics



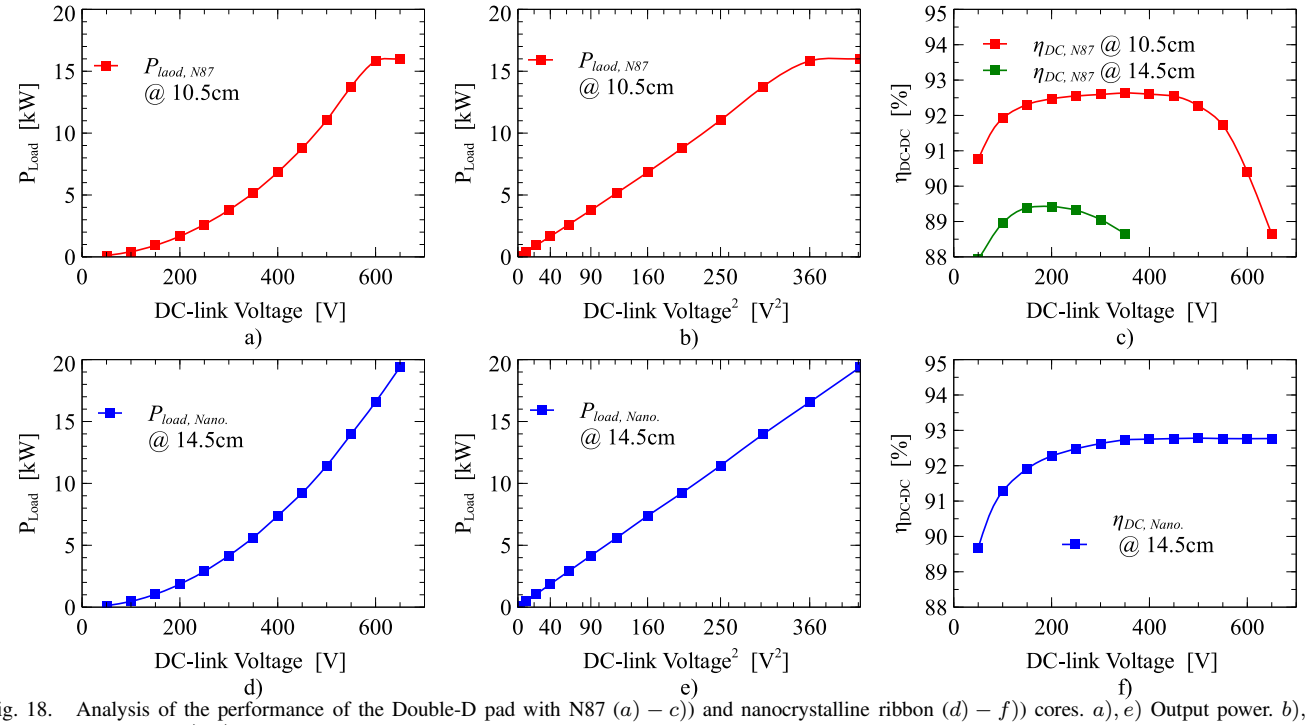


Fig. 18. Analysis of the performance of the Double-D pad with N87 $(a)-c))$ and nanocrystalline ribbon $(d)-f))$ cores. $a), e)$ Output power. $b), d)$ Linearized out power. $c), f)$ System's efficiency.

$\sim$600 V result in almost no additional power. More power can be transferred using using nanocrystalline ribbon cores as compared to ferrite cores of the same dimensions. Even at $>$ 22kW (double of its rating) the pad remained unsaturated. This leads to higher power densities.

For an unsaturated pad, the system's efficiency usually increases along with the power transfer and it flattens for higher power ratings, as shown in Fig.18$f$). For the nanocrystalline ribbon cores an efficiency of 93 % was achieved at a clearance of 14.5 cm. At the same clearance, the efficiency of the pad with ferrite cores is less than 90 % (Fig.18$c$)).

Due to saturation, the efficiency in ferrite pads does not flatten but rather plunges when saturation occurs due to two reasons. First, saturation produces a change in the effective coil inductance. As a result, the resonant frequency shifts, and the compensation circuit is no longer at resonance. This is can be seen in Fig.17$b$) when comparing the phase shift between current and voltage waveforms. Second, the current waveform is no longer sinusoidal. Contrarily, it depicts large peaks which result in higher copper losses, and can lead to failure of the power electronic components.

In Fig.18, the temperature was kept close to 25 °C at all times since the saturation point is temperature-dependent. For ferrite, it decays rapidly as the temperature increases as shown in Fig.19$a$). For most ferrites, the saturation point halves for temperatures between 100 and 150 °C. The rate of decay is slower for nanocrystalline alloys. Even at 200 °C, the saturation point decreases by less than 20%, as seen in Fig.19$a$). Therefore, nanocrystalline ribbon cores have an advantage over ferrite cores since they can withstand operation at high temperatures. The effect of temperature on the efficiency of the magnetic coupler is discussed in Section V-F.

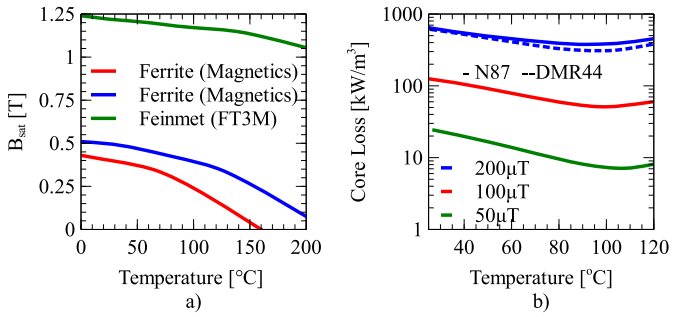


Fig. 19. $a)$ Saturation flux density for nanocrystalline ribbon FT-3M [18], and MnZn ferrites [24] versus temperature. $b)$ Core losses vs. temperature for different MnZn ferrites: N87 and DMR44.

### *E. Nanocrystalline Ribbon vs. Ferrite: Flux Density and Temperature Distribution*

The flux distribution within the core cannot be easily measured. However, given that the power losses are correlated to the flux density, thermal images of the core can be used to estimate the flux distribution within them. For this purpose, the shield of the receiver pad was removed and thermal images were taken after a 5 min operation at 6.6 kW, before the system reached thermal equilibrium. orangeThis power rating was selected without loss of generality. Thermal images at the thermal equilibrium were also taken. The initial and ambient temperatures were 23 °C in all cases.

*a) Flux Distribution:* For the ferrite cores, Fig.20$a$), the temperature/flux distribution is more irregular than that obtained with FEM simulations. The heterogeneous flux distribution is due to the small air gaps between the tiles forming the core. Due to manufacturing tolerance, the air gaps between tiles are not identical despite being carefully placed and spaced. Thus, the flux density is higher where the gap between tiles is narrower. Localized heating is therefore found at these spots due to the concentration of magnetic flux. These hot-spots reduce the magnetic performance of the pad, its efficiency, and they can result in failure from thermal shock, as discussed in Section III-D. Similar spots can be seen in the thermal analysis presented in [20], [25].

This article has been accepted for publication in a future issue of this journal, but has not been fully edited. Content may change prior to final publication. Citation information: DOI 10.1109/TPEL.2021.3064902, IEEE Transactions on Power Electronics



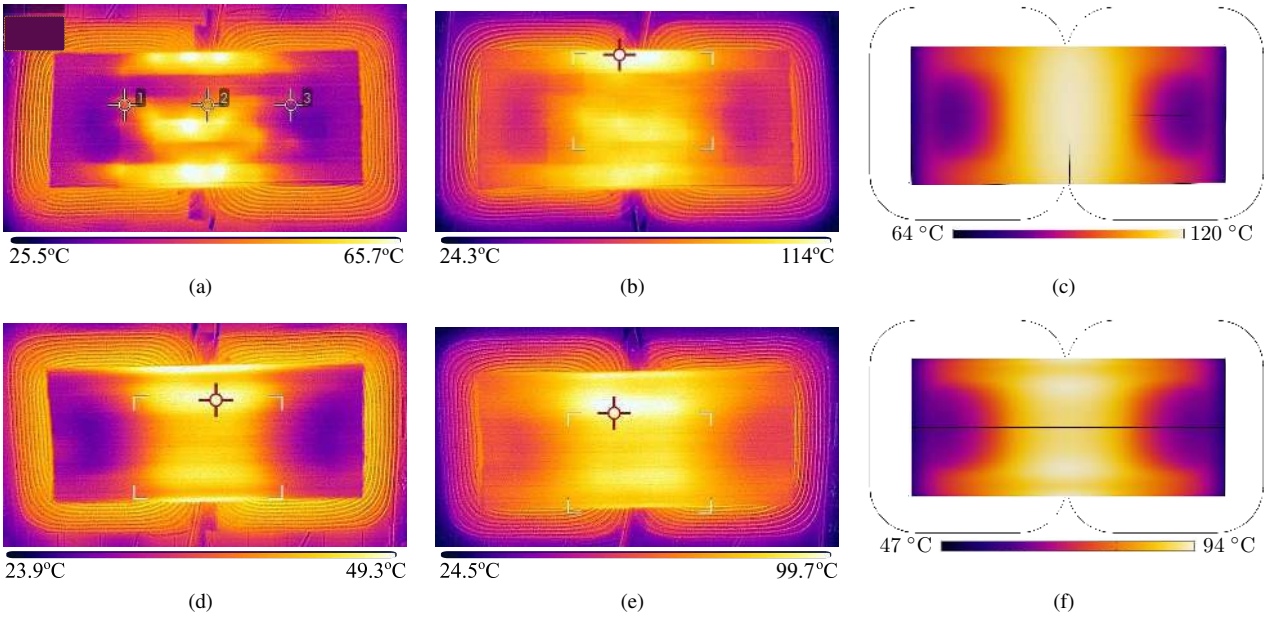


Fig. 20. Temperature distribution of the cores at 6.6 kW. $a)-c)$ correspond to the ferrite cores (tiles). $d)-f)$ correspond to the nanocrystalline ribbon cores. $a), d)$ Temperature distribution after a 5 min operation. $b), e)$ Temperature distribution at thermal equilibrium. $c), f)$ Simulation results at thermal equilibrium.

The flux/temperature distribution for the nanocrystalline ribbon cores, Fig.20$d$), agrees with FEM results shown in Fig.9. The top and bottom of the core show higher temperatures due to eddy-current losses. The upper part of the nanocrystalline ribbon core in Fig.20$d$) shows slightly higher temperatures. This asymmetry is attributed to manufacturing tolerances.The nanocrystalline cores used in this design are of bespoke design and made. Manufacture tolerances could be reduced for high volume production. A deeper analysis of the effect of the manufacturing tolerances on the performance of the pad is not presented in this work.

*b) Temperatures at thermal equilibrium:* Fig.20$b$) and Fig.20$e$) depict the thermal distribution in the cores at thermal equilibrium. At this condition, the temperature distribution in the core is more homogeneous compared to that at transient state. The maximum temperature in the ferrite core reaches 113 °C and 99.7 °C for the nanocrystalline ribbon core. The lower temperatures are due to the higher efficiency of the pad with nanocrystalline ribbon cores. FEA thermal simulations ares shown in Fig.20$c$) and Fig.20$f$). The estimated temperatures are in the same range as the measured ones for both core material. However, a more uniform profile was expected from both pads. Nonetheless, as explained before, the air gaps between the ferrite core and the tolerances in the nanocrystalline cores reduce the uniformity of the temperature distribution.

The temperature in the $x$-axis is less homogeneous in the ferrite core compared to that of the nanocrystalline ribbon cores. The maximum temperature difference across the core is approximately 55 °C. This large difference is attributed to the lower thermal conductivity of the ferrite which is worsened by the air gaps between the tiles. Contrarily, the maximum temperature difference within the nanocrystalline ribbon core was measured as approximately 40 °C. The lower temperature gradient is attributed to the lower cores losses as well as due to the higher thermal conductivity of the ribbon. The higher thermal conductivity of the nanocrystalline ribbon and the lack of air gaps enhance the heat dissipation and allows for a more uniform heat distribution in the $x$-axis.

*c) Effect of shielding plate in heat dissipation:* The aluminum shield functions as a heat-sink and improves the thermal performance of the pads. The shield helps to spread the heat which results in lower and more homogeneous temperatures in the core. When using the shield, two thermocouples were used to estimate the temperatures at the center and the edge of the core as seen in Fig.11(a) (TC). Temperature differences of 12.5 °C and 13.1 °C were measured for the nanocrystalline and ferrite pads, respectively. These are much lower than the ones obtained without the shield.

### *F. Nanocrystalline Ribbon vs. Ferrite: Performance vs. Temperature*

The performance of the pad versus temperature was evaluated by measuring the power transfer and the efficiency of the pad during operation. To disregard the effect of temperature on the power electronics, only the power across the pads are measured. The air gap between the transmitter and the receiver pads is set to 100 mm and the initial power transfer is set at 6.6 kW. At time $t = 0$, the power transfer begins while both pads are kept at ambient temperature (25 °C). The temperature in the core increases as a result of the core and coil losses. The system is run for approximately 75 min, the point at which the variation of temperature versus time was lower than 0.1 °C/min. The core temperature, shown in Fig.21$a$), was measured with a thermocouple placed at its center of the pad, below the coil.

Fig.21$b$) shows the power received at the load for a fixed DC-link voltage. The power received in the secondary increase with the time. This increase is due to the lower mutual inductance produced by the reduction of the core's permeability with the rising temperature (see (6)). A 2.2% variation of power is seen for the system that uses ferrite cores whereas a 1% variation is measured for the one with nanocrystalline cores, as seen in Fig.21$c$). The latter is therefore more stable to temperature variations.

This article has been accepted for publication in a future issue of this journal, but has not been fully edited. Content may change prior to final publication. Citation information: DOI 10.1109/TPEL.2021.3064902, IEEE Transactions on Power Electronics



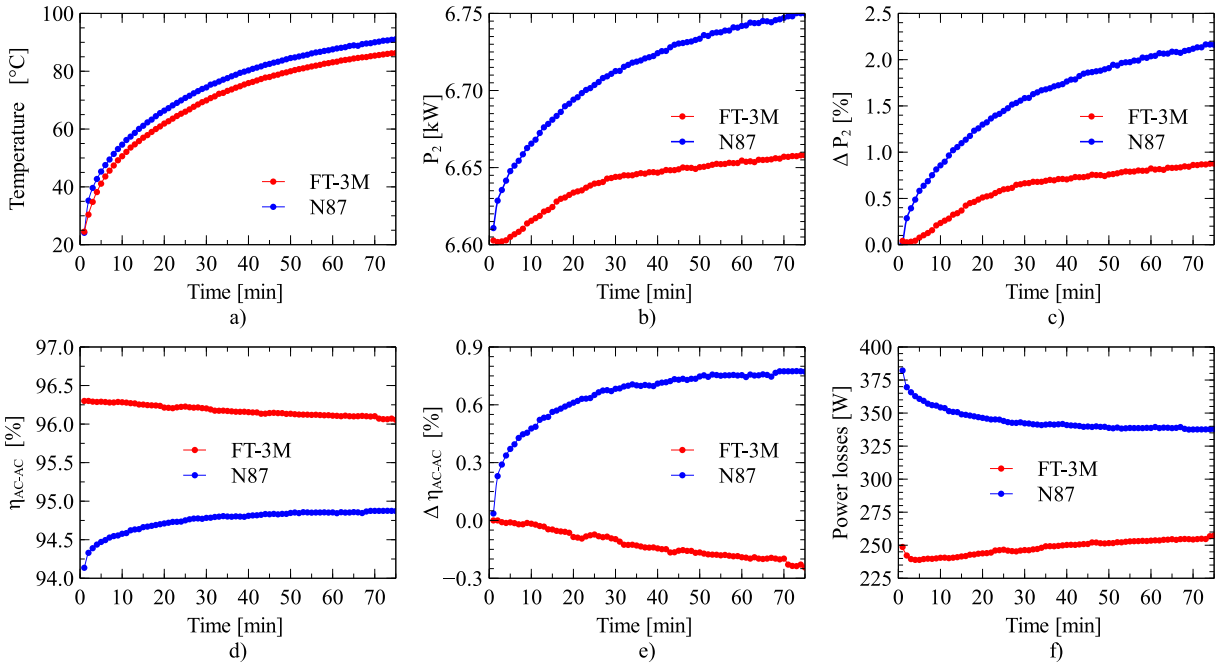


Fig. 21. Pad performance vs. Time/Temperature. $a$) Measurement of the temperature at the center of the core. $b$) Power transfer and $c$) its variation versus time/temperature. $d$) Pad's efficiency and $e$) its variation versus time/temperature. $f$) Power losses.

Fig.21$d$) shows the pad's efficiency versus time. The efficiency of the ferrite pad increases with the temperature. This is because hysteresis losses in ferrite decrease with the temperature, as seen in Fig.19$b$). This decline, however, only holds for temperatures below $\sim$100 °C. From this point onward, hysteresis losses increase once again which drives the efficiency down. During the studied interval, the efficiency increased by approximately 0.85%, as seen in Fig.21$e$). During the same interval, the efficiency of the pad with nanocrystalline cores reduces by about 0.3%. However, even with this reduction, the efficiency of the nanocrystalline pad is $\sim$ 1.2% higher than that of the ferrite pad. This is more clearly seen when comparing the power losses in the pad, depicted in Fig.21$f$). The higher losses result in higher operating temperature, as seen in Fig.21$a$). Due to the uneven distribution of temperature in the cores, a temperature-controlled chamber is required to analyze the performance of the pad at specific temperatures, particularly, for high operating temperatures. This analysis is not presented in this paper and it is suggested as future work.

### *G. Nanocrystalline Ribbon Core Segregation*

This section analyses the effect of core segmentation by considering gaps of 5, 10, and 15 mm between nanocrystalline ribbon core bars. Fig.22$a$) and Fig.22$b$) show the 6 cores that constitute the core with different separations between them.

The results agree with the simulations. Increasing the separation between the cores reduces the power transfer capability of the pad as shown in Fig.22$c$). Moreover, the increase in power loss leads to lower overall efficiencies as seen in Fig.22$d$).

These results are confirmed by the thermal images of the pads shown in Fig.23. The core temperature increases with the separation between cores. The thermal images were taken after a 5 min operation at 3.3 kW with an ambient temperature of 23 °C. In both cases, the highest temperatures are located at the lateral faces of the cores where higher eddy-currents and magnetic flux densities are present (see Fig.3).

From these results, one can conclude that the use of segregated cores in IPT pads with nanocrystalline cores

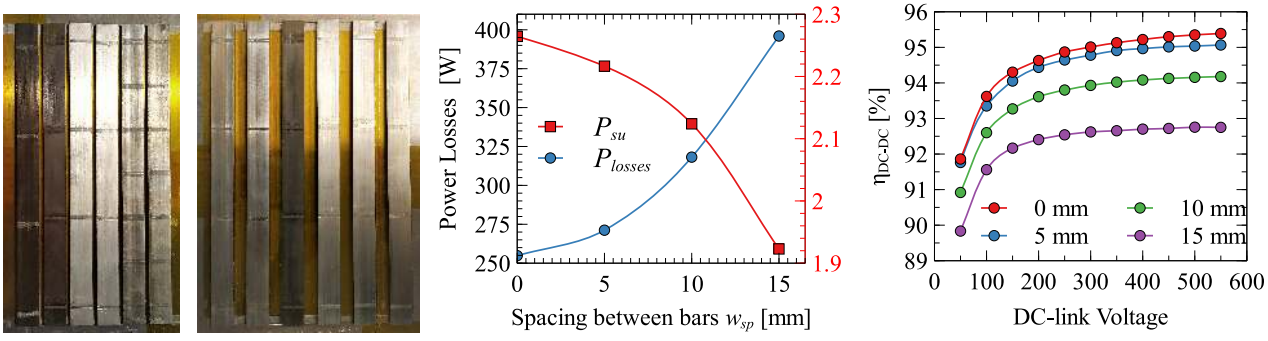


Fig. 22. Analysis of the spacing between core bars on the power transfer capability of the pad $P_{su}$, total system losses $P_{losses}$, and efficiency $\eta_{DC-DC}$. Six bars are considered, each of 4 mm×25 mm×342 mm. Depiction of the bars with different spacing between cores: $a$) 5 mm and $b$) 15 mm. $c$) $P_{su}$ and power losses. $d$) System's efficiency. $w_{sp}$ : Spacing between bars. $P_{su}$ @ $i_{1,pk}$ =21 A.

This article has been accepted for publication in a future issue of this journal, but has not been fully edited. Content may change prior to final publication. Citation information: DOI 10.1109/TPEL.2021.3064902, IEEE Transactions on Power Electronics



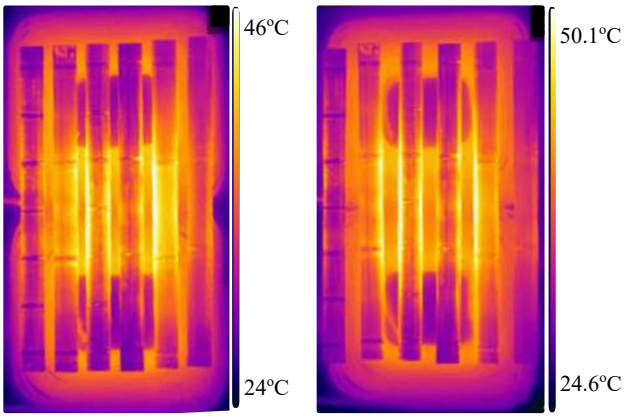


Fig. 23. Temperature distribution of the cores after operation at 3.3 kW for 5 min. Separation between cores: $a$) 10 mm and $a$) 15 mm.

is not effective. Keeping the cores together forming one equivalent core plate helps to reduce eddy-current losses. One can argue that using a core plate as opposed to core bars requires more magnetic material. However, this is incorrect as the thickness of the core can be reduced to keep the volume of core material constant −provided that the core remains unsaturated.

## VI. Conclusions and Outlook

Nanocrystalline ribbons cores can be used in IPT systems to increase their power density and robustness [9]. However, eddy-current losses are a limit factor which can drastically reduce the system's efficiency. Addressing this issue, this paper presents considerations and guidelines for the adequate design of nanocrystalline cores in IPT systems. Following these guidelines, eddy-current losses can be drastically reduced. Moreover, designs with higher power densities and efficiencies are possible. For validation, a WPT3 pad is designed and tested. For reference and comparison, an identical pad with ferrite cores has been also tested. Giving that the pad was optimized for nanocrystalline cores, the performance of the ferrite is inevitably sub-optimal. However, its testing serves as a reference point for the evaluation of the pad with nanocrystalline cores. The main findings of this paper are:

- The flux entering the lateral faces of the nanocrystalline ribbon cores −and producing excessive eddy-current losses− can be mitigated by reducing the core thickness, increasing the area coverage of the core, or increasing the number of cores. An area coverage greater than $\sim 60\%$ is recommended.
- For nanocrystalline alloys, a non-segregated core plate by placing individual cores together without spaces is preferred as the area exposed to perpendicular flux is reduced as well as the associated core losses.
- Using the proposed design method, nanocrystalline ribbon cores can outperform ferrite cores of the same dimensions, in terms of higher coupling factors, power levels, efficiency, power density, and thermal stability. A $2\%$ higher efficiency and $13\%$ higher coupling factor were measured.
- When the core saturates, the efficiency drops due to the change in the power factor and the non-sinusoidal current waveform. Nanocrystalline cores have a higher saturation point than ferrite. Thus, they offer a higher power transfer capability; i.e., higher power density.
- A ferrite core plate has to be constituted of many pieces due to high brittleness. The air gaps between pieces compromise the magnetic performance of the pad. They can lead to uneven flux distributions and hot-spots. Nanocrystalline ribbon cores do not have this problem as they can be fabricated as single-pieces structures. This leads to a superior magnetic and thermal performance in the direction of the main magnetic flux ($x$-axis).
- Nanocrystalline cores show a superior thermal performance compared to ferrite cores: a more uniform temperature distribution and a more gradual variation of permeability/power transfer versus temperature. As opposed to ferrite, however, the power losses increase with the temperature. Nonetheless, the rate of change is low.

As future work, an analysis of the performance of nanocrystalline ribbon cores at high temperatures is recommended. For this a temperature-controlled chamber is required. A comparative analysis of a system optimized for nanocrystalline ribbon cores versus one optimized for ferrite cores is suggested. Finally, an economic analysis, which considers the cost of nanocrystalline ribbon cores in mass production, is also suggested.

## References

[1] M. Budhia, G. A. Covic, and J. T. Boys, "Design and optimization of circular magnetic structures for lumped inductive power transfer systems," *IEEE Transactions on Power Electronics*, vol. 26, no. 11, pp. 3096–3108, Nov 2011.

[2] U. I. R. Bosshard and J. W. Kolar, "Comprehensive evaluation of rectangular and double-d coil geometry for 50 kw/85 khz ipt system," *IEEE Journal of Emerging and Selected Topics in Power Electronics*, vol. 4, no. 4, pp. 1406–1415, Dec 2016.

[3] M. Budhia, J. T. Boys, G. A. Covic, and C. Y. Huang, "Development of a single-sided flux magnetic coupler for electric vehicle ipt charging systems," *IEEE Transactions on Industrial Electronics*, vol. 60, no. 1, pp. 318–328, Jan 2013.

[4] R. Bosshard, "Multi-objective optimization of inductive power transfer systems for ev charging," Ph.D. dissertation, ETH Zurich, 2015.

[5] D. S. Deepak Bhalla, "Material processing technology for soft ferrites manufacturing," *American Journal of Materials Science*, vol. 6, pp. 165–170, 2013.

[6] M. Mohammad and S. Choi, "Optimization of ferrite core to reduce the core loss in double-d pad of wireless charging system for electric vehicles," in *2018 IEEE Applied Power Electronics Conference and Exposition (APEC)*. IEEE, 2018, pp. 1350–1356.

[7] T. Yilmaz, N. Hasan, R. Zane, and Z. Pantic, "Multi-objective optimization of circular magnetic couplers for wireless power transfer applications," *IEEE Transactions on Magnetics*, vol. 53, no. 8, pp. 1–12, 2017.

[8] A. Delgado, G. Salinas, J. Rodriguez, J. A. Oliver, and J. A. Cobos, "Finite element modelling of litz wire conductors and compound magnetic materials based on magnetic nano-particles by means of equivalent homogeneous materials for wireless power transfer system," in *2018 IEEE 19th Workshop on Control and Modeling for Power Electronics (COMPEL)*, June 2018, pp. 1–5.

[9] D. E. Gaona, S. Ghosh, and T. Long, "Feasibility study of nanocrystalline-ribbon cores for polarized inductive power transfer pads," *IEEE Transactions on Power Electronics*, vol. 35, no. 7, pp. 6799–6809, 2020.

[10] H. A. Davies and M. R. Gibbs, "Amorphous alloys," *Handbook of Magnetism and Advanced Magnetic Materials*, 2007.

[11] J. Füzer, S. Dobák, and P. Kollár, "Magnetization dynamics of fecunbsib soft magnetic ribbons and derived powder cores," *Journal of Alloys and Compounds*, vol. 628, pp. 335–342, 2015.

[12] Y. Wang, G. Calderon-Lopez, and A. J. Forsyth, "High-frequency gap losses in nanocrystalline cores," *IEEE Transactions on Power Electronics*, vol. 32, no. 6, pp. 4683–4690, June 2017.

This article has been accepted for publication in a future issue of this journal, but has not been fully edited. Content may change prior to final publication. Citation information: DOI 10.1109/TPEL.2021.3064902, IEEE Transactions on Power Electronics




[13] G. A. Covic and J. T. Boys, "Inductive power transfer," *Proceedings of the IEEE*, vol. 101, no. 6, pp. 1276–1289, 2013.

[14] R. Bosshard, J. W. Kolar, J. Mhlethaler, I. Stevanovi, B. Wunsch, and F. Canales, "Modeling and$\eta$-$\alpha$-pareto optimization of inductive power transfer coils for electric vehicles," *IEEE Journal of Emerging and Selected Topics in Power Electronics*, vol. 3, no. 1, pp. 50–64, March 2015.

[15] J. Wang, H. Lin, Y. Huang, and X. Sun, "A new formulation of anisotropic equivalent conductivity in laminations," *IEEE Transactions on Magnetics*, vol. 47, no. 5, pp. 1378–1381, May 2011.

[16] J. Ziske1, H. Neubert, and R. Disselnkoetter, "Modeling of anisotropic laminated magnetic cores using homogenization approaches," in *2014 COMSOL Conference in Cambridge*, 2014.

[17] VACUUMSCHMELZE, "Vitroperm vp 800 / 500," https://vacuumschmelze.de/Assets-Web/VITROPERMRep., 2019.

[18] Hitachi, "Nanocrystalline soft magnetic material finemet," https://www.hitachi-metals.co.jp/products/elec/tel/pdf/hl-fm9-h.pdf, Tech. Rep., 2016.

[19] Hitachi, "Nanocrystalline fe-based soft magnetic material with high saturation flux density and low core loss," https://elnamagnetics.com/wp-content/uploads/catalogs/Finemet/FINEMETTech. Rep., 2007.

[20] C. Boys, John; Grant, "Current distribution and thermal regulation in inductive power transfer coupling structures," *Patent WO2018097739A1.*, 2019.

[21] M. G. S. Pearce, "Inductive power transfer magnetics for roadways," Ph.D. dissertation, The University of Auckland, New Zealand, 2020.

[22] G. R. Kalra, M. G. S. Pearce, S. Kim, D. J. Thrimawithana, and G. A. Covic, "Measuring the q-factor of ipt magnetic couplers," in *2019 IEEE PELS Workshop on Emerging Technologies: Wireless Power Transfer (WoW)*, 2019, pp. 34–38.

[23] J. Schneider, "Wireless power transfer for light-duty plug-in/electric vehicles and alignment methodology," *SAE International J2954 Taskforce*, 2016.

[24] Magnetics, "Designing with magnetic cores at high temperatures," https://www.mag-inc.com/Design/Design-Guides/Designing-with-Magnetic-Cores-at-High-Temperatures, Tech. Rep., 2018.

[25] S. Kim, M. Amirpour, G. Covic, and S. Bickerton, "Thermal characterisation of a double-d pad," in *2019 IEEE PELS Workshop on Emerging Technologies: Wireless Power Transfer (WoW)*, 2019, pp. 1–5.


**Daniel E. Gaona** (SM'14) received the B.S. degree in electrical engineering and the B.S. degree in mechanical engineering from the University of San Francisco (Quito, Ecuador) in 2013 and 2014, respectively. In 2016, he received the M.Sc. degree in electrical engineering from the Erasmus Mundus Master Course (EMMC) Consortium. In 2017, he worked at the Department of Power Electronics and Electrical Drives at the University of Paderborn, Germany, as a Research Associate. In 2018, he joined the University of Cambridge for his Ph.D. degree where he has been rewarded with CAPE Acorn Blue Sky Research Award at University of Cambridge. His research interests include electric drives, power electronics, and wireless charging systems.

**Chaoqiang Jiang** (M19) received the B.Eng. and M.Eng. degrees in electrical engineering and automation from Wuhan University, Wuhan, China, in 2012 and 2015, respectively, and the Ph.D. degree in electrical and electronic engineering from The University of Hong Kong, Hong Kong, in 2019. He is currently an Assistant Professor with the Department of Electrical Engineering, City University of Hong Kong, Hong Kong SAR, China. He was a Postdoctoral Research Associate at University of Cambridge, U.K. Also, he is affiliated with Clare Hall Cambridge from 2021. In 2019, he was a Visiting Researcher at the Nanyang Technological University, Singapore. His research interests include power electronics, wireless power transfer techniques, electric machines and drives, and electric vehicle (EV) technologies. Dr. Jiang is currently an Associate Editor of IET Renewable Power Generation. He has been rewarded with the Winner, CAPE Acorn Blue Sky Research Award at University of Cambridge, and First Prize in the Interdisciplinary Research Competition at University of Hong Kong.

**Teng Long** (M'13) received the B.Eng. degree from the Huazhong University of Science and Technology, China, the first class B.Eng. (Hons.) degree from the University of Birmingham, UK in 2009, and the Ph.D. degree from the University of Cambridge, UK in 2013. Until 2016, he was a Power Electronics Engineer with the General Electric (GE) Power Conversion business in Rugby, UK. He is currently a Lecturer with the University of Cambridge. His research interests include power electronics, electrical machines, and machine drives. Dr Long is a Chartered Engineer (CEng) registered with the Engineering Council in the UK.